Supporting Information

Stable Radical Cations Based on Indolo[3,2,1-jk]carbazole: Synthesis, Characterization, and Theoretical Calculation

Jiayao Yang,[a] Linlin Yang,[a] Tao Li,*[a] and Wanxiang Zhao,*[a]

State Key Laboratory of Chemo and Biosensing, College of Chemistry and Chemical Engineering, Hunan University, Changsha, Hunan 410082, P. R. China

Email, zhaowanxiang@hnu.edu.cn, litao_0922@hnu.edu.cn

Table of contents

1. Materials and Measurements

All reagents were purchased from the commercial suppliers and used without further purification. Solvents were purified and dried following standard laboratory methods prior to use. Compounds **pICz**[1], **mICz**[2] and $Li[Al(OR^F)_4]$ (OR^F = $OC(CF_3)_3$)[3] were synthesized according to reported procedures. Anhydrous CH_2Cl_2 and n-hexane were obtained from Energy Chemical. $NOSbF_6$ and NO_2SbF_6 was purchased from Shanghai Aladdin Biochemical Technology Co., Ltd. All manipulations involving moisture- or air-sensitive compounds were carried out under under a nitrogen atmosphere using standard Schlenk techniques in oven-dried reaction vessels. Elemental analysis was performed on a Vario EL CUBE elemental analyzer. Thermogravimetric analysis (TGA) was conducted using a TGA 101 thermogravimetric analyzer, and differential scanning calorimetry (DSC) was carried out on a DZ-DSC300C differential scanning calorimeter. UV-vis-NIR absorption spectra were recorded on Hitachi U-4100 spectrophotometer. Electron paramagnetic resonance (EPR) spectra were measured on JEOL JES-FA200. X-ray diffraction data were collected on a Bruker D8 Venture diffractometer equipped with a Cu Kα radiation source (λ = 1.5406 Å). All structural solutions and refinements were performed using the SHELXL package within the OLEX2 software.

2. Synthetic Details

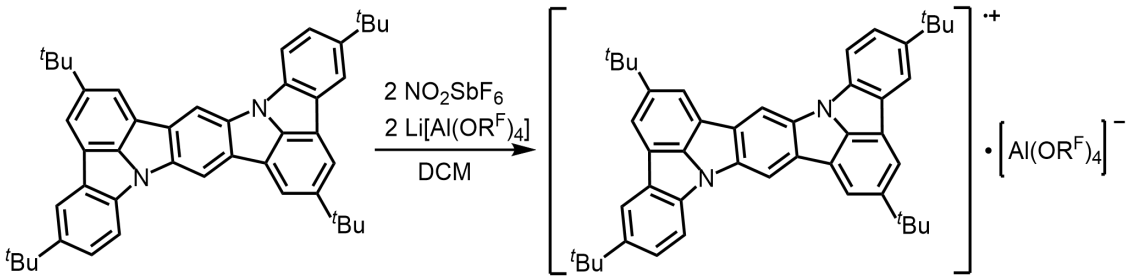

Syntheses of [**pICz**]$^{\bullet+}$[Al(OR^F)$_4$]$^-$: Under an inert atmosphere, the neutral precursor **pICz** (15 mg, 0.024 mmol), NO_2SbF_6 (13 mg, 0.046 mmol) and Li[Al(OR^F)$_4$] (46 mg，0.047 mmol) were placed in a 10 mL Schlenk flask. Then 5 mL CH_2Cl_2 was injected, and the mixture was stirred overnight. The resultant green solution was filtered to remove any precipitate. Crystallization was carried out by the slow diffusion of hexane into the CH_2Cl_2 solution at 4 ℃. After ten days, green crystals was obtained (21 mg，0.013 mmol，55% yield) . Elemental analysis calcd (%) for $C_{62}H_{48}AlF_{36}N_2O_4$: C 46.66, H 3.03, N 1.76; found: C 46.76, H 2.89, N 1.83.

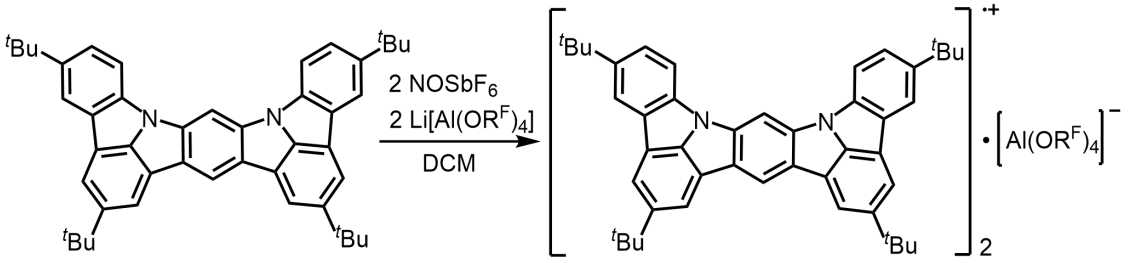

Syntheses of [**mICz**]$_2^{\bullet+}$[Al(OR^F)$_4$]$^-$: Under an inert atmosphere, the neutral precursor **mICz** (15 mg, 0.024 mmol), $NOSbF_6$ (13 mg, 0.046 mmol) and Li[Al(OR^F)$_4$] (46 mg，0.047 mmol) were placed in a 10 mL Schlenk flask. Then 5 mL CH_2Cl_2 was injected, and the mixture was stirred overnight. The resultant green solution was filtered to remove any precipitate. Crystallization was carried out by the slow diffusion of hexane into the CH_2Cl_2 solution at 4 ℃. After ten days, green crystals was obtained (24 mg，0.020 mmol，45%) . Elemental analysis calcd (%) for $C_{108}H_{96}AlF_{36}N_4O_4$: C 58.30, H 4.35, N 2.52; found: C 58.59, H 4.42, N 2.49.

3. Powder X-ray Diffraction

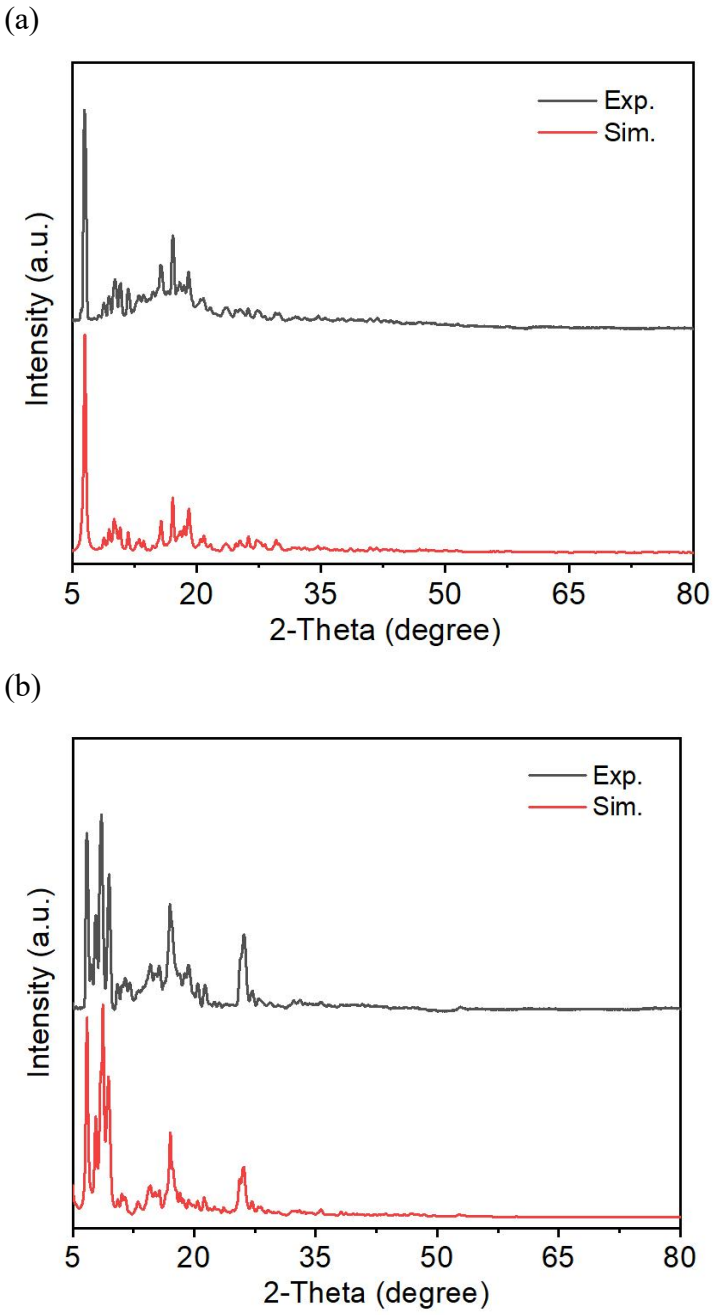

Fig. S1 Experimental and simulated PXRD patterns for compound (a) [**pICz**]$^{\bullet+}$[Al(OR^{F})$_4$]$^-$ and (b) [**mICz**]$_2^{\bullet+}$[Al(OR^{F})$_4$]$^-$.

4. Thermogravimetric and Differential Scanning Calorimetry

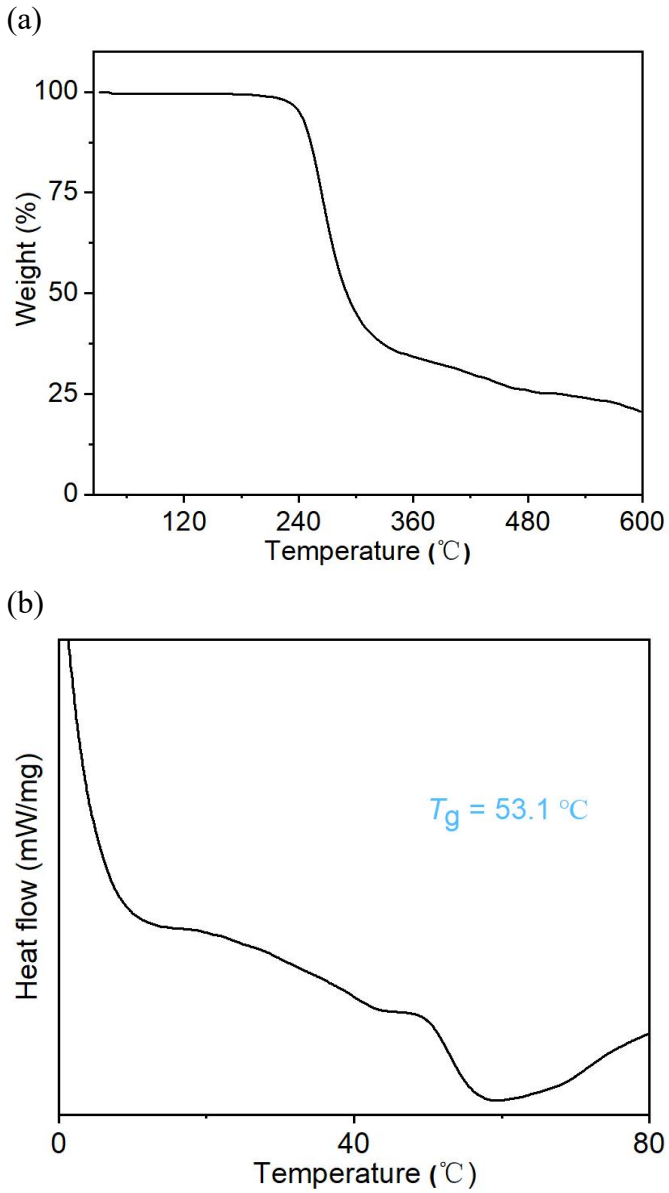

Fig. S2 (a) TGA and DSC analysis of radical cation [**pICz**]$^{\bullet+}$[Al(OR^F)$_4$]$^-$.

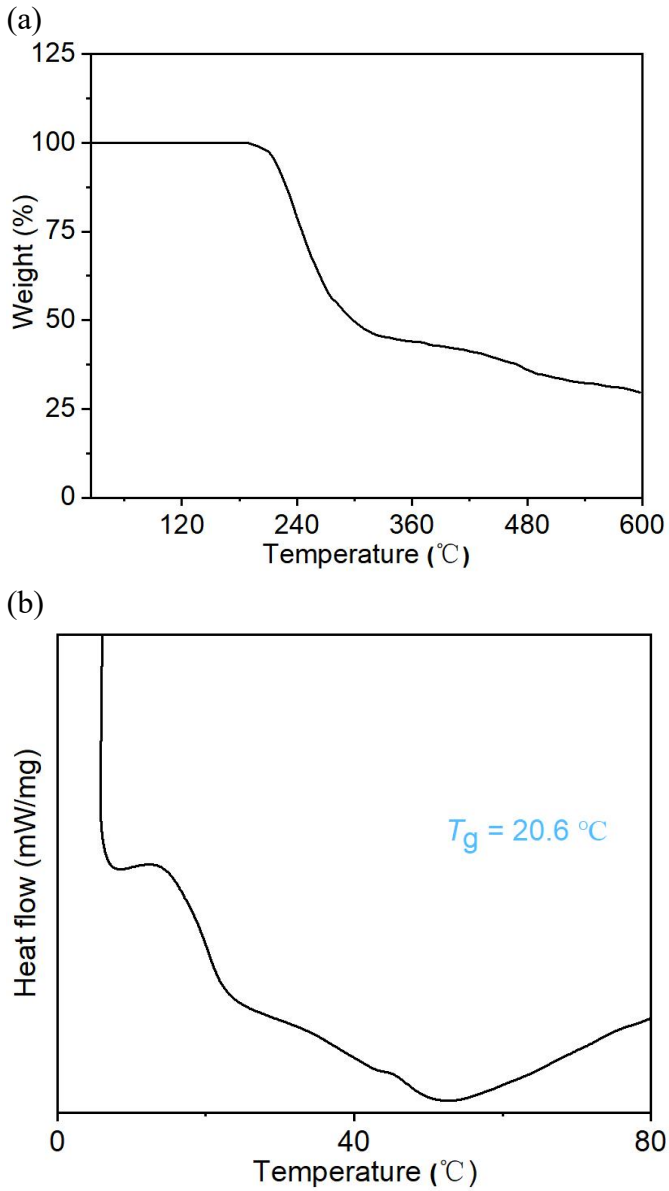

Fig. S3 (a) TGA and (b) DSC analysis of radical cation $[\mathbf{mICz}]_2^{\bullet+}[Al(OR^F)_4]^-$.

5. X-ray crystallographic data

Single crystal of [**pICz**]$^{\bullet+}$[Al(OR^F)$_4$]$^-$ and [**mICz**]$_2^{\bullet+}$[Al(OR^F)$_4$]$^-$ suitable for X-ray diffraction analysis was grown by slow diffusion of anhydrous n-hexane into their anhydrous CH_2Cl_2 solutions. X-ray diffraction data were collected on a Bruker D8 Venture diffractometer using Cu Kα radiation (λ = 1.54184 Å). Data were processed using SAINT and corrected for absorption with SADABS.[4] The structures were solved by direct methods and refined by full-matrix least-squares refinement on F^2 using SHELXS and SHELXL within the SHELXTL package.[5] All non-hydrogen atoms were refined anisotropically. Hydrogen atoms were placed in calculated positions and refined using a riding model. Crystallographic data have been deposited with the Cambridge Crystallographic Data Centre (CCDC) and can be obtained free of charge via www.ccdc.cam.ac.uk/data_request/cif.

Table S1. Crystal data and structure refinement

Identification code	[**pICz**]$^{\bullet+}$[Al(OR^F)$_4$]$^-$:	[**mICz**]$_2^{\bullet+}$[Al(OR^F)$_4$]$^-$
CCDC	2519779	2519780
Empirical formula	$C_{62}H_{48}AlF_{36}N_2O_4$	$C_{108}H_{96}AlF_{36}N_4O_4$
Formula weight	1596.00	2224.86
Crystal system	triclinic	monoclinic
Space group	P-1	C2/c
a/Å	11.5239(3)	48.7724(13)
b/Å	15.1374(3)	13.9285(4)
c/Å	19.9082(4)	39.1474(9)
α/°	106.1860(10)	90
β/°	100.0950(10)	124.3540(10)
γ/°	96.1510(10)	90
Volume/Å^3	3238.52(13)	21955.0(10)
Z	2	8
ρ_{calc} g/cm^3	1.637	1.346
μ (mm^{-1})	1.687	1.160
F(000)	1606.0	9128.0
Crystal size/mm^3	0.3 × 0.27 × 0.26	0.221 × 0.102 × 0.077
Radiation	CuKα (λ = 1.54178)	CuKα (λ = 1.54178)
2θ range for date collection	4.732 to 136.53	4.388 to 136.85
Index ranges	-11 ≤ h ≤ 13, -18 ≤ k ≤ 18, -23 ≤ l ≤ 23	-58 ≤ h ≤ 58, -16 ≤ k ≤ 13, -47 ≤ l ≤ 47
Reflection collected	61861	111881
Independent reflections	11808 [R_{int} = 0.0522, R_{sigma} = 0.0415]	20120 [R_{int} = 0.0718, R_{sigma} = 0.0496]
Data/restrains/parameters	11808/2444/1414	20120/1846/1729
Goodness-of-fit on F^2	1.045	1.040
Final R indexes (I>2σ(I))	R_1 = 0.0489, wR_2 = 0.1283	R_1 = 0.0940, wR_2 = 0.2660
Final R indexes [all data]	R_1 = 0.0576, wR_2 = 0.1316	R_1 = 0.1120, wR_2 = 0.2803
Largest diff. peak/hole/e Å^{-3}	0.80/-0.75	0.90/-0.63

Table S2 Selected bond lengths of [**pICz**]$^{\bullet+}$[Al(OR^{F})$_4$]$^-$ in single crystal structure.

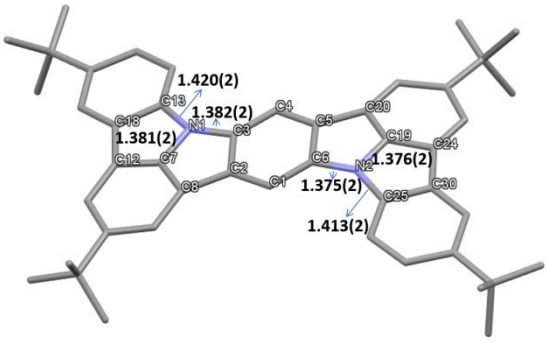

Chemical bond	Bond length (Å)	Chemical bond	Bond length (Å)
N1–C3	1.382(2)	N1–C7	1.381(2)
N1–C13	1.420(2)	N2–C6	1.375(2)
N2–C19	1.376(2)	N2–C25	1.413(2)
C1–C2	1.377(2)	C2–C3	1.452(2)
C3–C4	1.404(2)	C4–C5	1.385(2)
C5–C6	1.447(2)	C1–C6	1.401(2)
C2–C8	1.471(2)	C7–C8	1.368(2)
C7–C12	1.369(2)	C12–C18	1.474(2)
C13–C18	1.430(2)	C5–C20	1.475(2)
C19–C20	1.370(2)	C19–C24	1.376(2)
C24–C30	1.477(2)	C25–C30	1.423(2)

Table S3 Selected bond lengths of [**mICz**]$_2^{\bullet+}$[Al(OR^F)$_4$]$^-$ in single crystal structure.

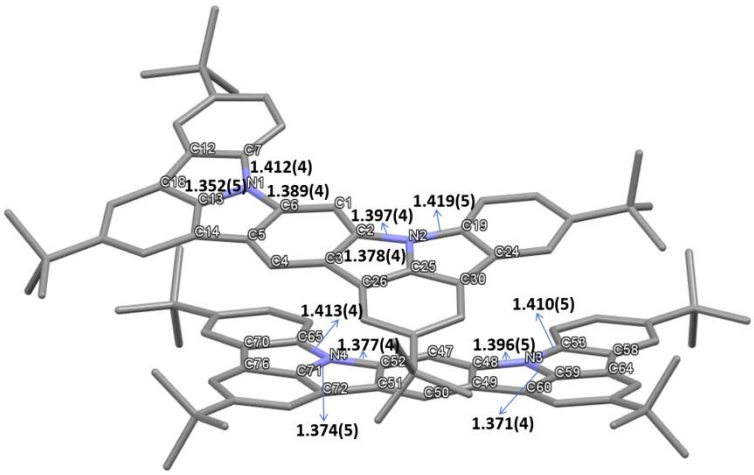

Chemical bond	Bond length (Å)	Chemical bond	Bond length (Å)
N1–C6	1.389(4)	N1–C7	1.412(4)
N1–C13	1.352(5)	N2–C2	1.397(4)
N2–C19	1.419(5)	N2–C25	1.378(4)
C1–C2	1.388(5)	C2–C3	1.450(5)
C3–C4	1.384(5)	C4–C5	1.405(5)
C5–C6	1.449(5)	C1–C6	1.386(5)
C5–C14	1.452(5)	C13–C14	1.382(5)
C13–C18	1.382(5)	C12–C18	1.477(5)
C7–C12	1.429(5)	C3–C26	1.479(4)
C25–C26	1.370(5)	C25–C30	1.367(5)
C24–C30	1.478(5)	C19–C24	1.424(5)
N3–C48	1.396(5)	N3–C53	1.410(5)
N3–C59	1.371(4)	N4–C52	1.377(4)
N4–C65	1.413(4)	N4–C71	1.374(5)
C47–C48	1.372(5)	C48–C49	1.458(5)
C49–C50	1.391(5)	C50–C51	1.389(5)
C51–C52	1.457(5)	C47–C52	1.397(5)
C49–C60	1.466(5)	C59–C60	1.357(5)
C59–C64	1.379(5)	C58–C64	1.471(5)
C53–C58	1.425(5)	C51–C72	1.464(5)
C71–C72	1.369(5)	C71–C76	1.377(5)
C70–C76	1.475(5)	C65–C70	1.432(5)

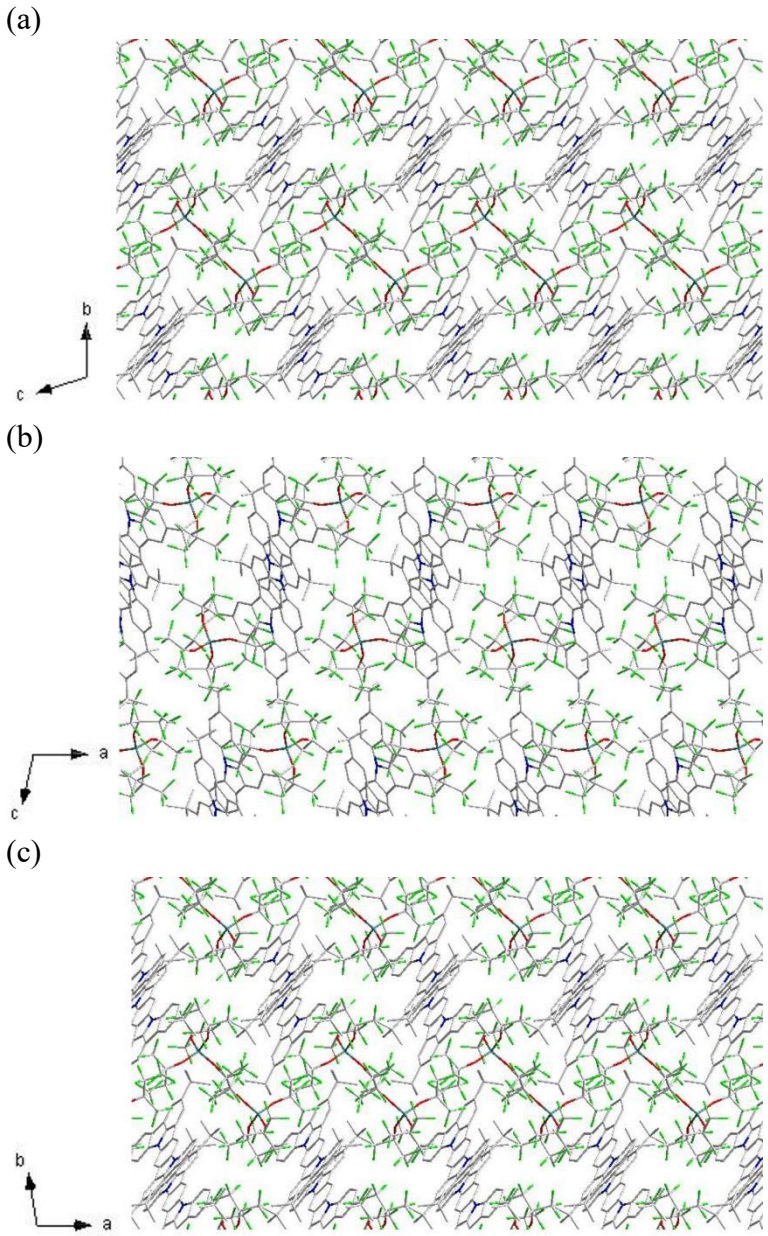

Fig. S4 Packing structure of [**pICz**]$^{\bullet+}$[Al(OR^{F})$_4$]$^-$ viewed along the (a) *a*-axis, (b) *b*-axis and (c) *c*-axis.

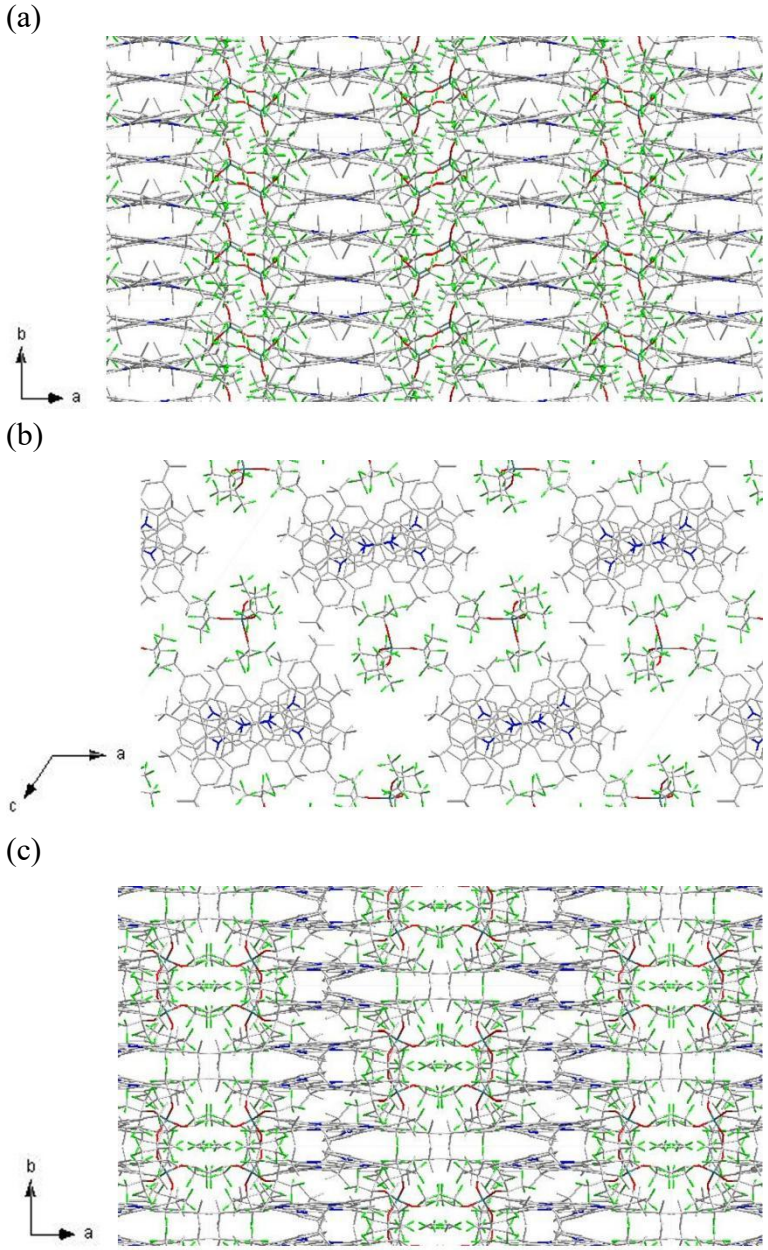

Fig. S5 Packing structure of [**mICz**]$_2^{\bullet+}$[Al(OR^F)$_4$]$^-$ viewed along the (a) *a*-axis, (b) *b*-axis and (c) *c*-axis.

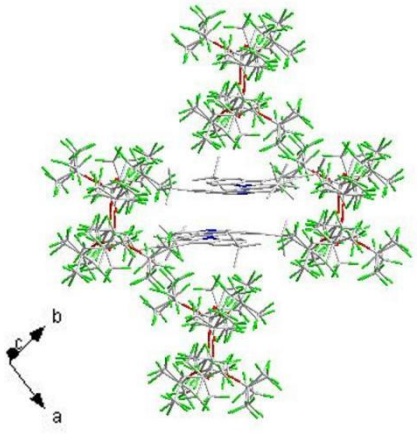

Fig. S6 Selected pairs of [**pICz**]$^{\bullet+}$ cations with pairs of [Al(OR^F)$_4$]$^-$ anions in the crystal structure of [**pICz**]$^{\bullet+}$[Al(OR^F)$_4$]$^-$ viewed along a non-crystallographic direction.

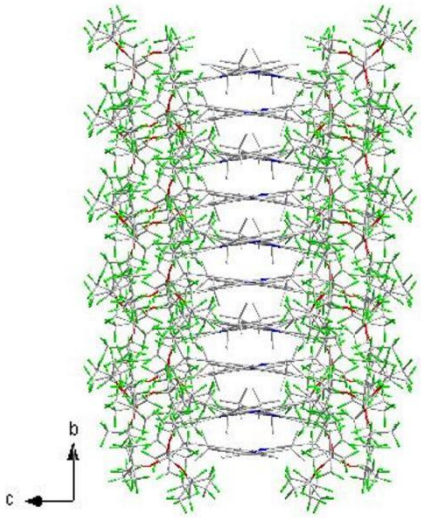

Fig. S7 Selected infinite columnarstacks of **mICz** separated by [Al(OR^F)$_4$]$^-$ anions in the crystal structure of [**mICz**]$_2^{\bullet+}$[Al(OR^F)$_4$]$^-$

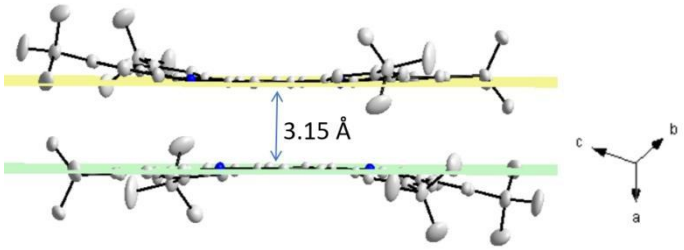

Fig. S8 Intermolecular distance between neighboring **pICz** core in [**pICz**]$^{\bullet+}$[Al(OR^F)$_4$]$^-$. The distance is defined as the perpendicular distance from the centroid of the central benzene ring to the mean plane of an adjacent cation. The shorter of the two such distances, arising from non-parallel layer stacking, is reported.

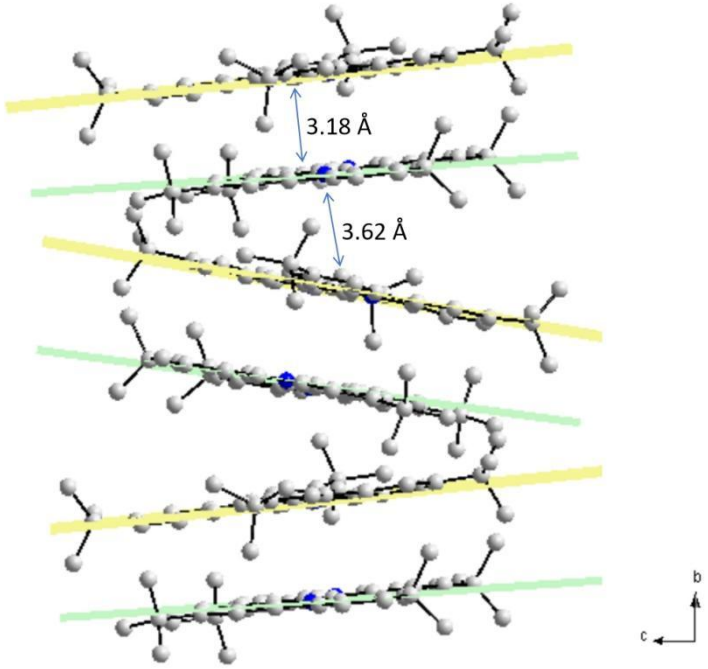

Fig. S9 Intermolecular distance between neighboring **mICz** core in [**mICz**]$_2^{\bullet+}$[Al(OR^F)$_4$]$^-$. The distance is defined as the perpendicular distance from the centroid of the central benzene ring to the mean plane of an adjacent cation. The shorter of the two such distances, arising from non-parallel layer stacking, is reported.

.

6. EPR characterization

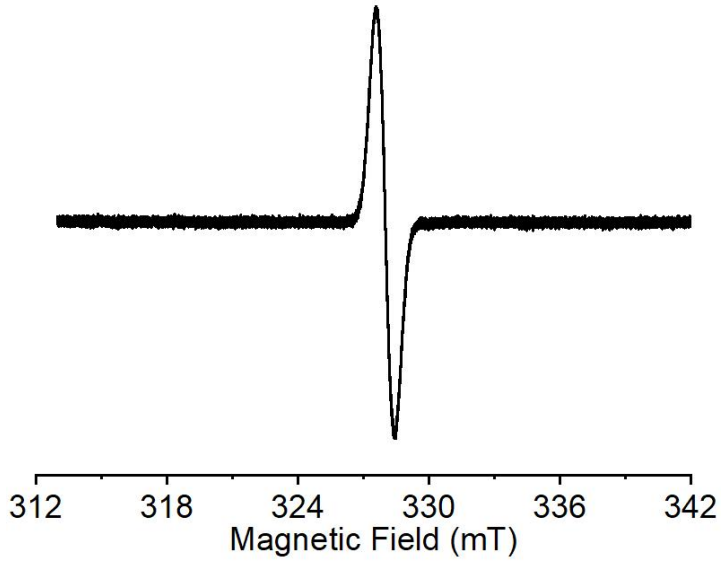

Fig. S10 The CW X-band EPR spectrum of the radical cation [**pICz**]$^{\bullet+}$[Al(OR^{F})$_4$]$^-$ (1.0 mM in dichloromethane) was measured at 298 K.

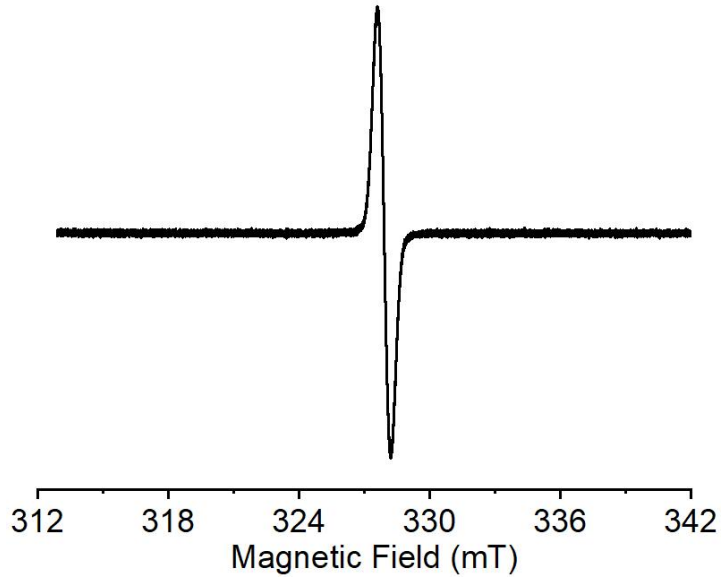

Fig. S11 The CW X-band EPR spectrum of the radical cation [**mICz**]$_2^{\bullet+}$[Al(OR^{F})$_4$]$^-$ (1.0 mM in dichloromethane) was measured at 298 K.

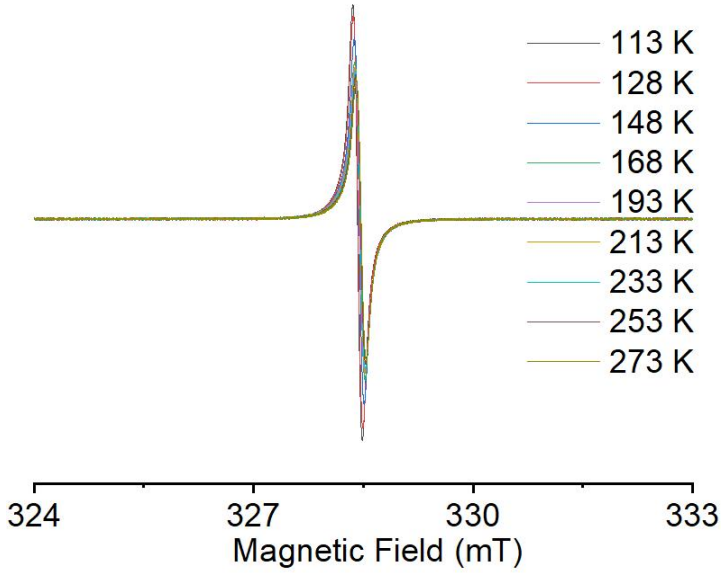

Fig. S12 Variable-temperature EPR spectra of the polycrystalline powder [**pICz**]$^{\bullet+}$•[Al(OR^{F})$_4$]$^-$ over the temperature range of 113–273 K.

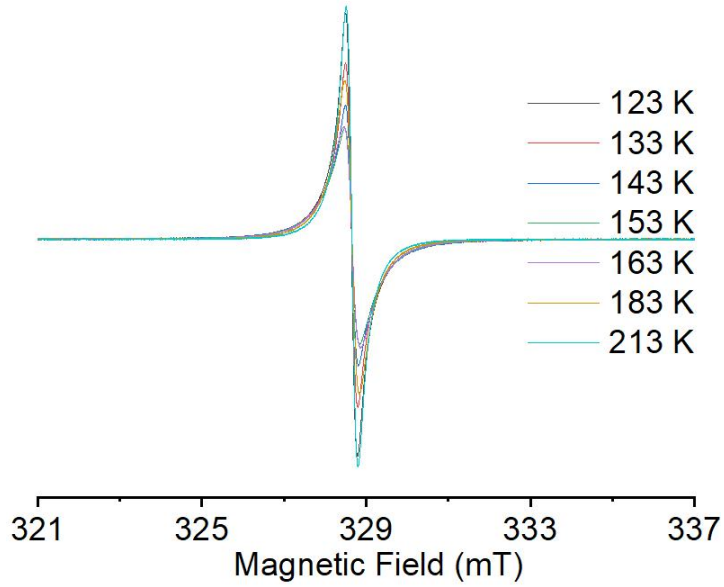

Fig. S13 Variable-temperature EPR spectra of the polycrystalline powder [**mICz**]$_2^{\bullet+}$•[Al(OR^{F})$_4$]$^-$ over the temperature range of 123–213 K.

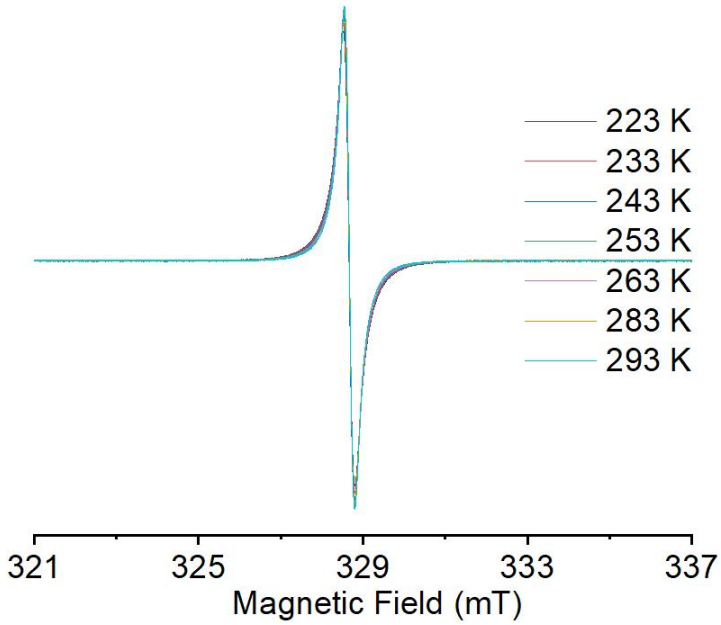

Fig. S14 Variable-temperature EPR spectra of the polycrystalline powder [**mICz**]$_2^{\bullet+}$•[Al(OR^F)$_4$]$^-$ over the temperature range of 223–293 K.

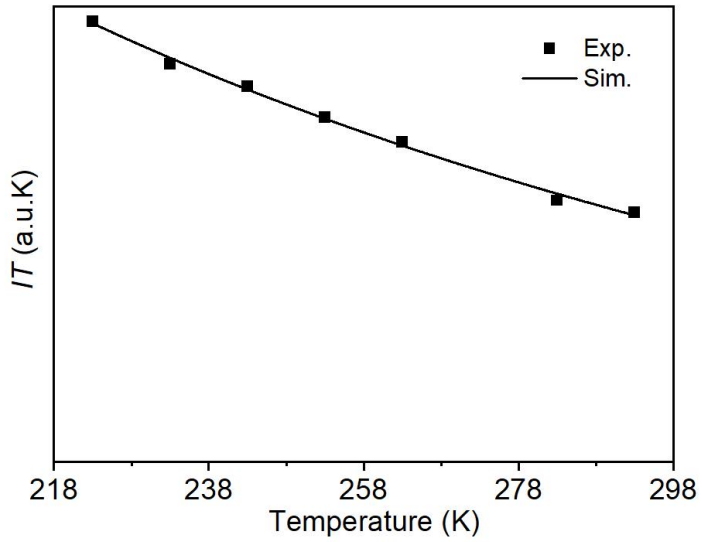

Fig. S15 Fitted *IT*-*T* curves for [**mICz**]$_2^{\bullet+}$[Al(OR^F)$_4$]$^-$ for variable-temperature EPR in polycrystalline state over the temperature range of 223–293 K. I: Integrated EPR intensity; T: temperature (in K).

7. Theoretical calculations

Theoretical calculations were performed using the Gaussian 16[6] and Multiwfn[7] software packages. The crystal structure was used as the initial geometry. Wavefunction files were subsequently generated for visualizing weak intermolecular interactions via the Independent Gradient Model based on Hirshfeld partition of molecular density (IGMH) method.[8] The corresponding isosurface maps were rendered using VMD 1.9.3,[9] based on cube files generated by Multiwfn. Geometry optimizations for all molecules in the ground state were conducted at the UB3LYP/6-31G(d) level. Time-dependent density functional theory (TD-DFT) calculations were then performed on the optimized geometries at the UM062X/6-31+G(d) level to obtain the simulated electronic absorption spectra.

(a)

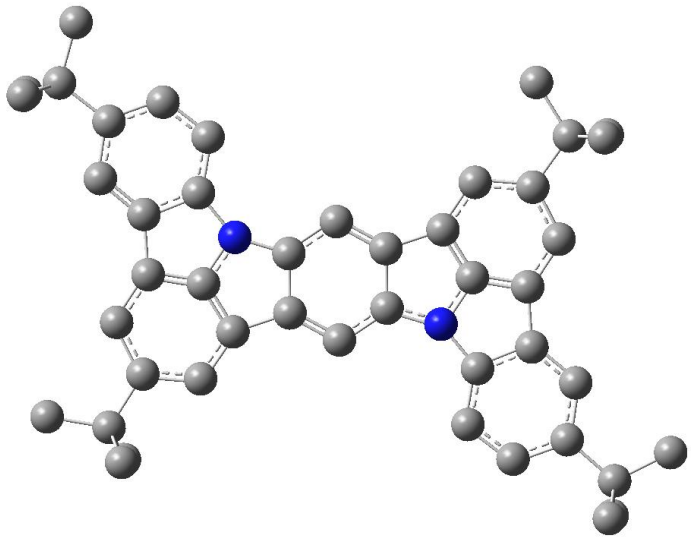

Top view

(b)

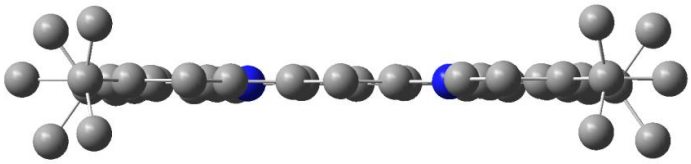

Side view

Fig. S16 Optimized molecular structures of [**pICz**]$^{\bullet+}$ calculated at the UB3LYP/6-31G(d) level in the gas phase.

(a)

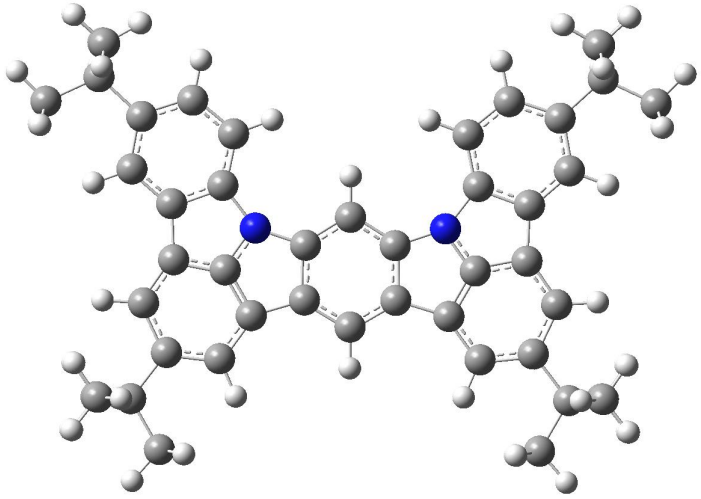

Top view

(b)

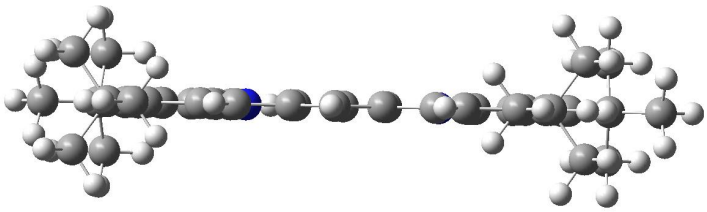

Side view

Fig. S17 Optimized molecular structures of [**mICz**]$^{\bullet+}$ calculated at the UB3LYP/6-31G(d) level in the gas phase.

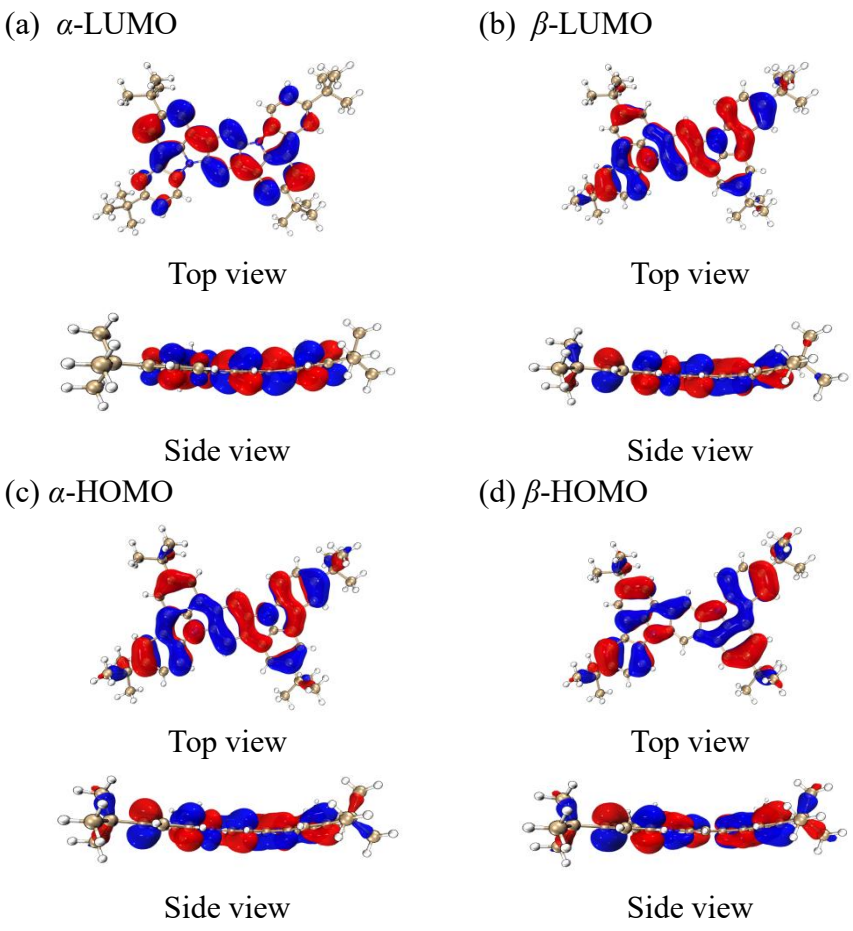

Fig. S18 Calculated frontier molecular orbital of [**pICz**]$^{\bullet+}$[Al(OR^{F})$_4$]$^-$ at the UB3LYP/6-31G(d) level (isovalue = 0.020).

(a) α-LUMO

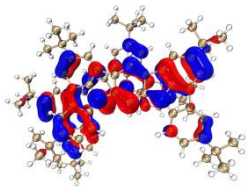

Top view

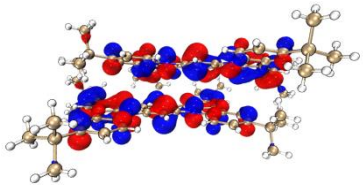

Side view

(b) β-LUMO

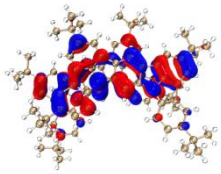

Top view

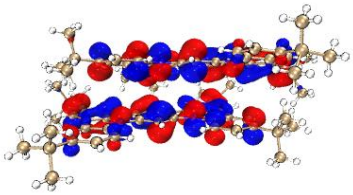

Side view

(c) α-HOMO

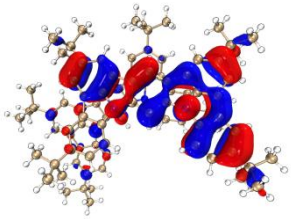

Top view

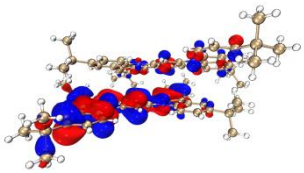

Side view

(d) β-HOMO

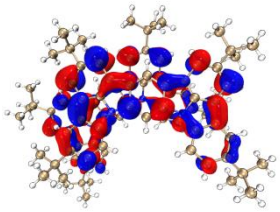

Top view

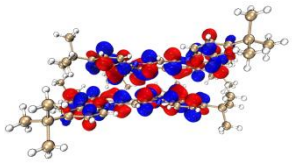

Side view

Fig. S19 Calculated frontier molecular orbital of [**mICz**]$_2^{\bullet+}$[Al(OR^F)$_4$]$^-$ at the UB3LYP/6-31G(d) level (isovalue = 0.020).

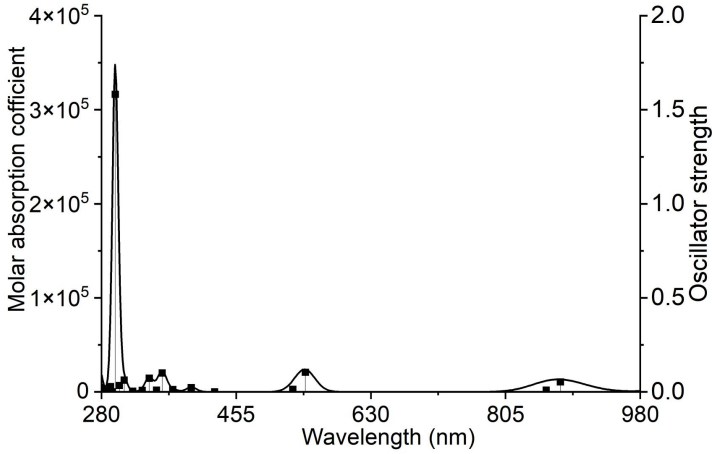

Fig. S20 TD-DFT calculated absorption spectrum of [**pICz**]$^{\bullet+}$ at the UM062X/6-31+G(d) level.

Table S4 Selected TD-DFT (UM062X/6-31+G(d)) calculated wavelength, oscillator strength, and compositions of major electronic transitions of [**pICz**]$^{\bullet+}$.

No.	Wavelength (nm)	Oscillator strength	Major contributions
1	876.08	0.053	HOMO-3(β)->LUMO(β)
2	544.81	0.104	HOMO-4(β)->LUMO(β) (90%),
3	528.49	0.0135	HOMO-5(β)->LUMO(β) (87%)
4	396.53	0.023	HOMO-7(β)->LUMO(β) (67%),
			HOMO-1(α)->LUMO(α) (8%),
			HOMO(α)->LUMO(α) (6%),
5	372.59	0.0126	HOMO-1(α)->LUMO(α) (36%),
			HOMO-7(β)->LUMO(β) (17%),
			HOMO-1(β)->LUMO+1(β) (22%)
6	358.83	0.1005	HOMO(α)->LUMO(α) (57%)
7	341.98	0.0723	HOMO-3(α)->LUMO(α) (18%),
			HOMO(α)->LUMO(α) (16%),
			HOMO-2(α)->LUMO+1(α) (7%)
8	309.46	0.0624	HOMO-21(β)->LUMO(β) (16%),
			HOMO-13(β)->LUMO(β) (29%),
			HOMO-1(β)->LUMO+1(β) (14%),
			HOMO(α)->LUMO+2(α) (7%)
9	303.11	0.0339	HOMO-1(α)->LUMO(α) (10%),
			HOMO(α)->LUMO+2(α) (24%),
			HOMO-13(β)->LUMO(β) (12%),
			HOMO-1(β)->LUMO+1(β) (19%)
10	297.79	1.5818	HOMO-1(α)->LUMO(α) (18%),
			HOMO(α)->LUMO+2(α) (36%),
			HOMO-1(β)->LUMO+1(β) (15%)
11	291.62	0.0276	HOMO(α)->LUMO+1(α) (24%),
			HOMO-4(α)->LUMO(α) (7%),
			HOMO-1(β)->LUMO+2(β) (7%),

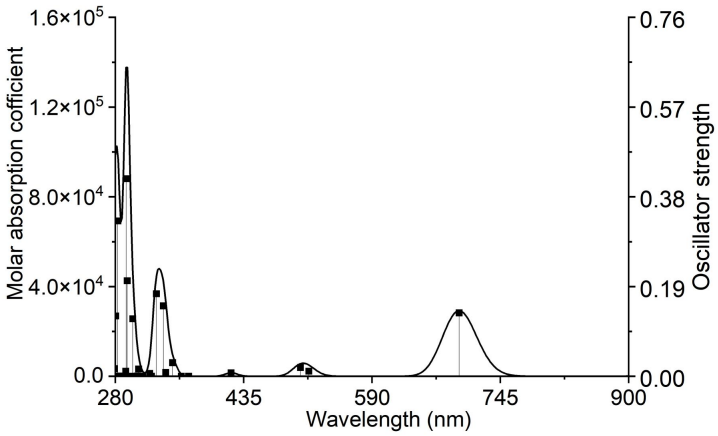

Fig. S21 TD-DFT calculated absorption spectrum of [**mICz**]$^{\bullet+}$ at the UM062X/6-31+G(d) level

Table S5 Selected TD-DFT (UM062X/6-31+G(d)) calculated wavelength, oscillator strength, and compositions of major electronic transitions of [**mICz**]$^{\bullet+}$.

No.	Wavelength (nm)	Oscillator strength	Major contributions
1	695.25	0.1342	HOMO-4(β)->LUMO(β) (94%)
2	513.64	0.0109	HOMO-6(β)->LUMO(β) (28%), HOMO-5(β)->LUMO(β) (60%)
3	503.49	0.0187	HOMO-6(β)->LUMO(β) (61%), HOMO-5(β)->LUMO(β) (32%)
4	349.07	0.0288	HOMO-3(α)->LUMO(α) (12%), HOMO-2(β)->LUMO+1(β) (13%), HOMO-1(α)->LUMO(α) (8%), HOMO-8(β)->LUMO(β) (9%),
5	338.00	0.1492	HOMO(α)->LUMO(α) (48%), HOMO(α)->LUMO+1(α) (13%), HOMO(β)->LUMO+1(β) (8%)
6	329.49	0.1747	HOMO-1(α)->LUMO(α) (14%), HOMO-1(β)->LUMO+2(β) (12%), HOMO-4(α)->LUMO+1(α) (7%), HOMO(α)->LUMO(α) (8%), HOMO(α)->LUMO+1(α) (9%),
7	308.06	0.0154	HOMO-21(β)->LUMO(β) (27%), HOMO-14(β)->LUMO(β) (28%)
8	300.90	0.1218	HOMO-1(α)->LUMO(α) (26%), HOMO(β)->LUMO+1(β) (24%), HOMO(β)->LUMO+2(β) (19%)
9	294.27	0.2023	HOMO-1(α)->LUMO+1(α) (10%), HOMO-1(β)->LUMO+1(β) (19%), HOMO-16(β)->LUMO(β) (9%), HOMO(β)->LUMO+2(β) (9%),
10	293.08	0.4184	HOMO(α)->LUMO+1(α) (10%),

			HOMO-1(β)->LUMO+1(β) (24%),
			HOMO-16(β)->LUMO(β) (8%),
11	292.45	0.0108	HOMO(β)->LUMO+2(β) (26%),
			HOMO-1(α)->LUMO(α) (7%),
			HOMO-1(β)->LUMO+2(β) (7%),
13	282.89	0.3289	HOMO-19(β)->LUMO(β) (15%),
			HOMO-16(β)->LUMO(β) (12%),
			HOMO-1(β)->LUMO+2(β) (16%),
			HOMO-1(α)->LUMO+1(α) (8%),
14	280.26	0.1277	HOMO-19(β)->LUMO(β) (10%),
			HOMO-1(β)->LUMO+2(β) (16%)

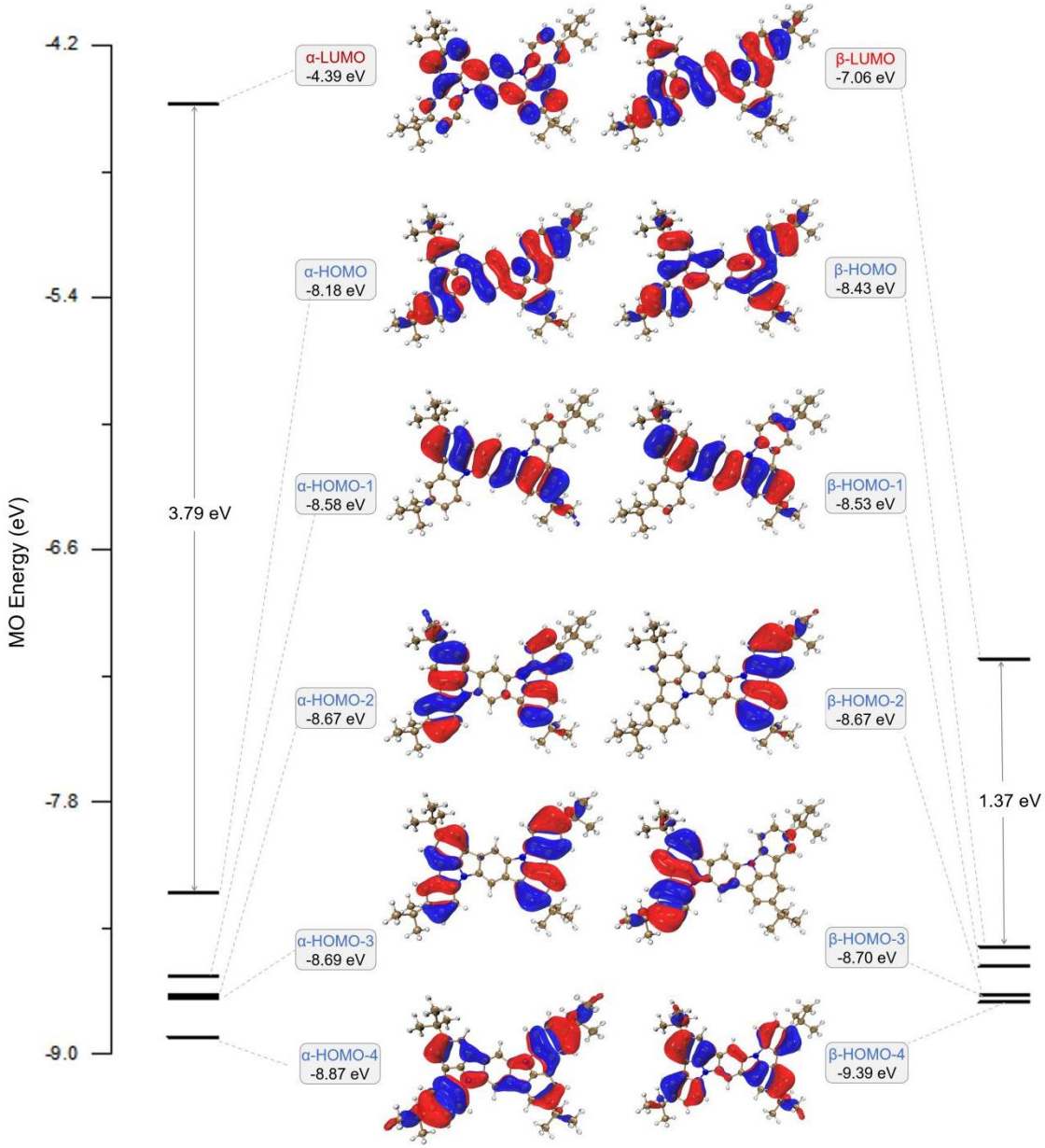

Fig. S22 Selected molecular orbitals, and the energy diagram of [**pICz**]$^{\bullet+}$[Al(OR^{F})$_4$]$^-$ obtained from DFT calculations.

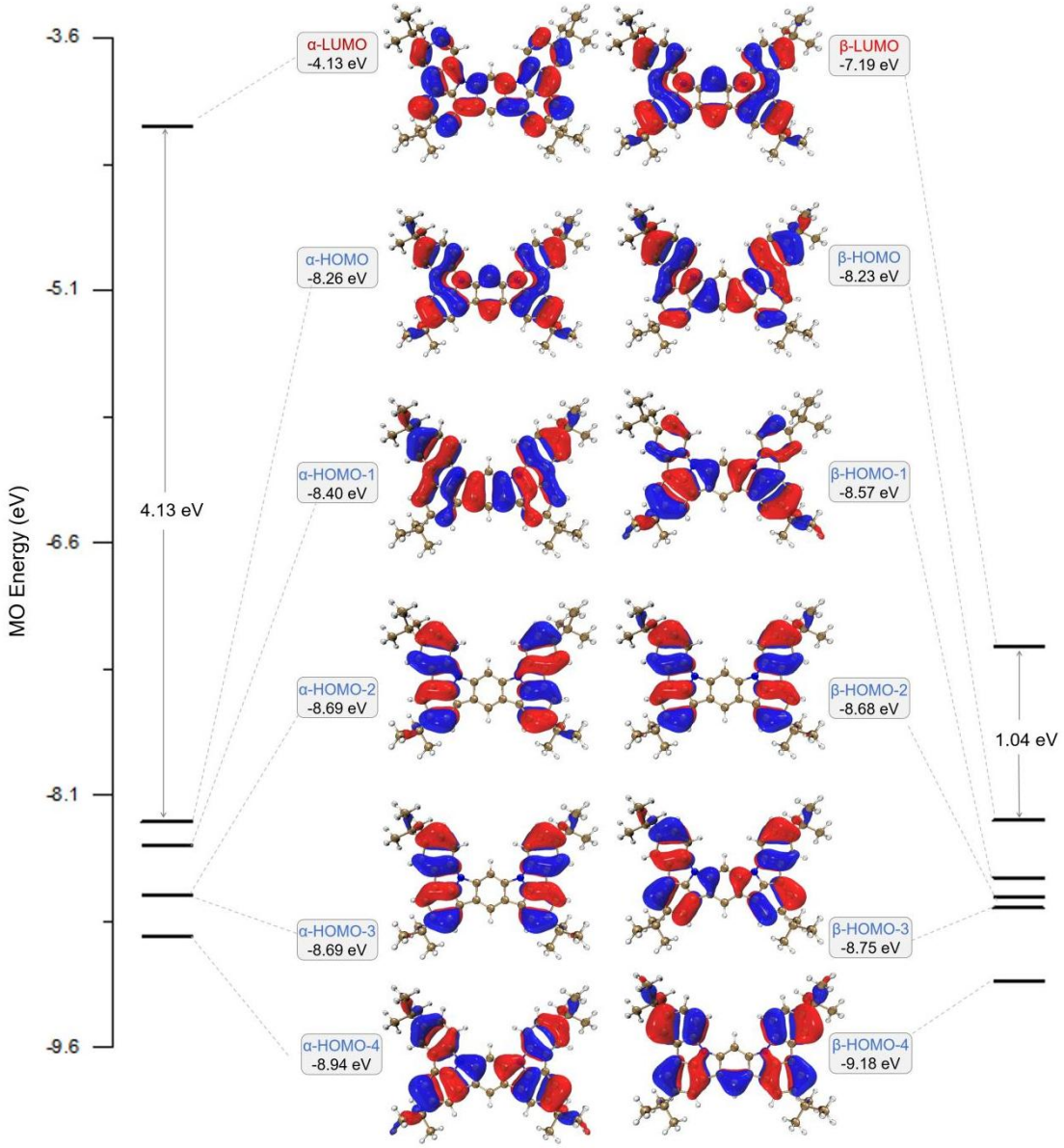

Fig. S23 Selected molecular orbitals, and the energy diagram of [**mICz**]$_2^{\bullet+}$[Al(OR^F)$_4$]$^-$ obtained from DFT calculations.

(a)

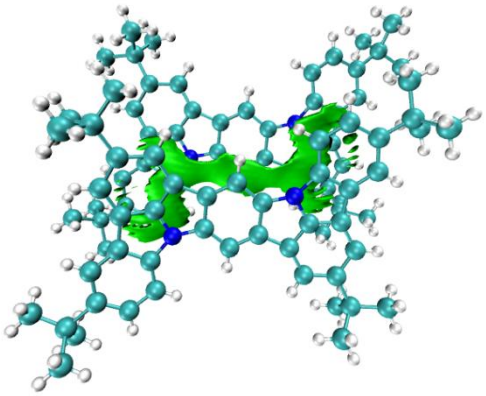

(b)

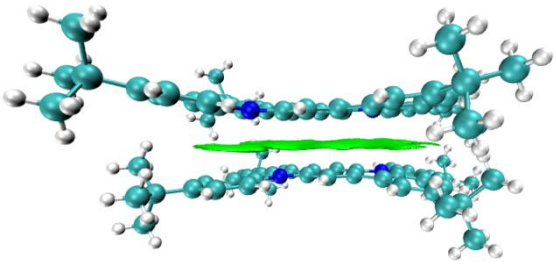

Fig. S24 IGMH analysis of the noncovalent interactions in [**pICz**]$^{\bullet+}$[Al(OR^{F})$_4$]$^-$ based on its crystal structure (δg^{inter} = 0.004).

(a)

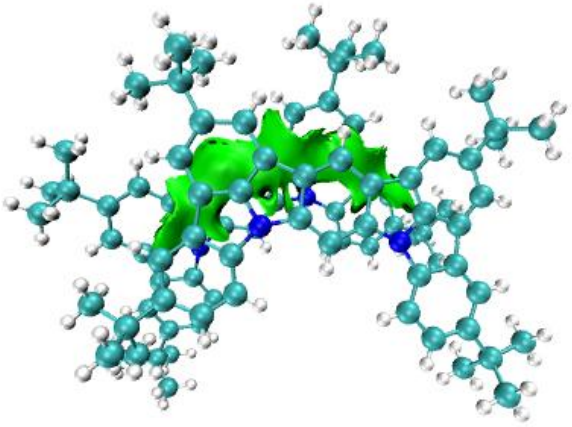

(b)

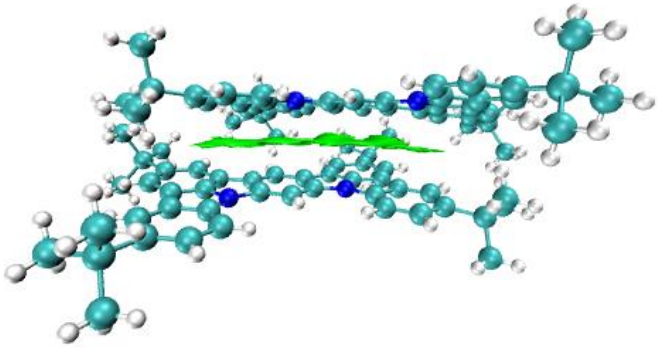

Fig. S25 IGMH analysis of the noncovalent interactions in $[\mathbf{mICz}]_2^{\bullet+}[Al(OR^F)_4]^-$ based on its crystal structure ($\delta g^{inter} = 0.004$).

(a)

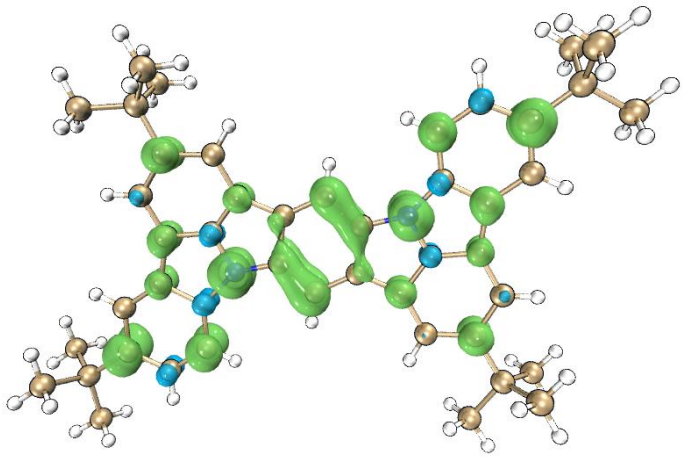

(b)

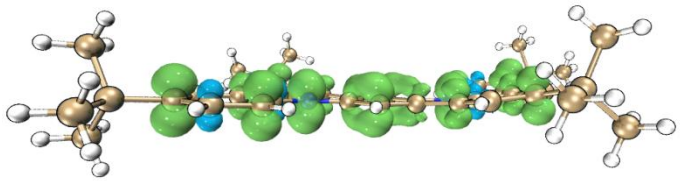

Fig. S26 Calculated spin densities of [**pICz**]$^{\bullet+}$[Al(OR^{F})$_4$]$^-$ at the UB3LYP/6-31G(d) level (isovalue = 0.004). Green and blue surfaces represent α and β spin densities, respectively.

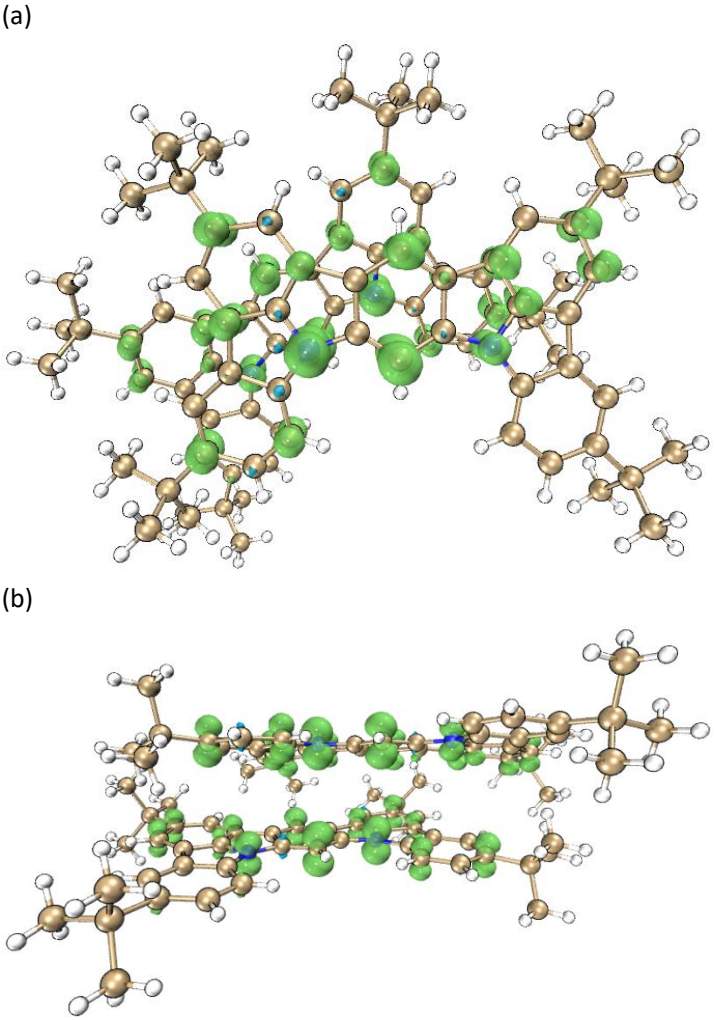

Fig. S27 Calculated spin densities of [**mICz**]$_2^{\bullet+}$[Al(OR^F)$_4$]$^-$ at the UB3LYP/6-31G(d) level (isovalue = 0.004). Green and blue surfaces represent α and β spin densities, respectively.

Table S6 Charge distribution data for [**pICz**]$^{\bullet+}$[Al(OR^{F})$_4$]$^-$

Number	Element	Mulliken charges
1	N	-0.765984
2	N	-0.755007
3	C	0.341185
4	C	0.034939
5	C	0.144319
6	C	0.135338
7	C	0.004714
8	C	0.333337
9	C	0.358529
10	C	0.209546
11	C	-0.02631
12	C	0.200368
13	C	0.343224
14	C	-0.159919
15	C	-0.023022
16	C	0.184203
17	C	-0.127681
18	C	-0.00889
19	C	-0.147131
20	C	0.202864
21	C	0.021361
22	C	0.016897
23	C	-0.14039
24	C	-0.105646
25	C	0.220071
26	C	0.192836
27	C	-0.156549
28	C	0.185789
29	C	0.187578
30	C	-0.054401
31	C	-0.083724
32	C	0.023337
33	C	-0.04422
34	C	-0.08402
35	C	-0.091863
36	C	0.045944
37	C	-0.082193
38	C	0.039285
39	C	0.035887
40	C	0.049281
41	C	0.041377
42	C	0.04637
43	C	0.049408
44	C	0.033477
45	C	0.037836
46	C	0.046787
47	C	0.045945
48	C	0.044922

Table S7 Charge distribution data for two mICz units in $[\mathbf{mICz}]_2^{\bullet+}[Al(OR^F)_4]^-$

No.	Element	Mulliken charges	No.	Element	Mulliken charges
1	N	-0.783092	1	N	-0.794922
2	N	-0.781064	2	N	-0.782268
3	C	0.355319	3	C	0.214138
4	C	0.219833	4	C	0.159288
5	C	0.346483	5	C	-0.171926
6	C	-0.023514	6	C	0.208238
7	C	-0.155485	7	C	-0.196333
8	C	0.153741	8	C	0.225057
9	C	0.209239	9	C	-0.188534
10	C	0.1752	10	C	0.14198
11	C	0.356043	11	C	0.180761
12	C	0.01563	12	C	-0.031488
13	C	0.161298	13	C	0.370512
14	C	-0.079287	14	C	0.355934
15	C	-0.189596	15	C	0.22069
16	C	0.00224	16	C	0.339592
17	C	-0.0151	17	C	0.01895
18	C	0.331493	18	C	0.346352
19	C	-0.024711	19	C	-0.08104
20	C	0.031809	20	C	-0.078576
21	C	-0.01173	21	C	-0.005915
22	C	-0.171993	22	C	-0.027832
23	C	0.202138	23	C	0.181766
24	C	0.19045	24	C	-0.053541
25	C	-0.0608	25	C	0.012591
26	C	-0.173897	26	C	-0.026151
27	C	0.212887	27	C	-0.003819
28	C	-0.13622	28	C	-0.187205
29	C	-0.190399	29	C	0.040137
30	C	0.183048	30	C	-0.138329
31	C	-0.081842	31	C	-0.084341
32	C	-0.062307	32	C	0.179736
33	C	0.183522	33	C	0.032374
34	C	-0.081058	34	C	-0.079571
35	C	0.039439	35	C	0.192906
36	C	-0.082582	36	C	-0.163431
37	C	0.046332	37	C	-0.064021
38	C	0.034867	38	C	0.022713
39	C	0.025306	39	C	0.041582
40	C	0.038958	40	C	0.024321
41	C	0.026577	41	C	0.025746
42	C	0.02464	42	C	0.019831
43	C	-0.081349	43	C	0.043964
44	C	0.023206	44	C	-0.079551
45	C	0.026136	45	C	0.029328
46	C	0.022826	46	C	0.03147
47	C	0.048457	47	C	0.023029
48	C	0.017344	48	C	0.037379

8. References

1 J. Wei, C. Zhang, D. Zhang, Y. Zhang, Z. Liu, Z. Li, G. Yu, and L. Duan, *Angew. Chem. Int. Ed.*, 2021, **60**, 12269–12273.

2 T. Taniguchi, Y. Itai, Y. Nishii, N. Tohnai and M. Miura, *Chem. Lett.*, 2019, **48**, 1160–1163.

3 I. Krossing, *Chem. Eur. J.* 2001, **7**, 490–502.

4 SMART and SADABS. Bruker AXS Inc., Madison, 1997.

5 G. Sheldrick, *Acta Crystallogr. Sect. A*, 2015, **71**, 3.

6 Gaussian 16, Revision C.01, M. J. Frisch, G. W. Trucks, H. B. Schlegel, G. E. Scuseria, M. A. Robb, J. R. Cheeseman, G. Scalmani, V. Barone, G. A. Petersson, H. Nakatsuji, X. Li, M. Caricato, A. V. Marenich, J. Bloino, B. G. Janesko, R. Gomperts, B. Mennucci, H. P. Hratchian, J. V. Ortiz, A. F. Izmaylov, J. L. Sonnenberg, D. Williams-Young, F. Ding, F. Lipparini, F. Egidi, J. Goings, B. Peng, A. Petrone, T. Henderson, D. Ranasinghe, V. G. Zakrzewski, J. Gao, N. Rega, G. Zheng, W. Liang, M. Hada, M. Ehara, K. Toyota, R. Fukuda, J. Hasegawa, M. Ishida, T. Nakajima, Y. Honda, O. Kitao, H. Nakai, T. Vreven, K. Throssell, J. A. Montgomery, Jr., J. E. Peralta, F. Ogliaro, M. J. Bearpark, J. J. Heyd, E. N. Brothers, K. N. Kudin, V. N. Staroverov, T. A. Keith, R. Kobayashi, J. Normand, K. Raghavachari, A. P. Rendell, J. C. Burant, S. S. Iyengar, J. Tomasi, M. Cossi, J. M. Millam, M. Klene, C. Adamo, R. Cammi, J. W. Ochterski, R. L. Martin, K. Morokuma, O. Farkas, J. B. Foresman, and D. J. Fox, Gaussian, Inc., Wallingford CT, 2016.

7 T. Lu and F. Chen, *J. Comput. Chem.*, 2012, **33**, 580–592.

8 T. Lu and Q. Chen, *J. Comput. Chem.*, 2022, **43**, 539–555.

9 W. Humphrey, A. Dalke and K. Schulten, *J. Molec. Graphics*, 1996, **14**, 33–38.